Monte Carlo Simulation of Leakage Currents in TiN/ZrO_2/TiN Capacitors

Gunther Jegert, Alfred Kersch, Wenke Weinreich, and Paolo Lugli, *Senior Member, IEEE*

***Abstract*—Leakage currents in TiN/high-κ-ZrO_2/TiN capacitors were simulated by using a novel kinetic Monte Carlo algorithm specially designed to describe tunneling transport of charge carriers in high-κ dielectrics, including defect-assisted transport mechanisms. Comparing simulation results with experimental data, a model for electronic transport was established and validated. Transport was found to be dominated by Poole–Frenkel emission from positively charged bulk trap states at medium voltages and trap-assisted tunneling at high voltages. Information on the conduction band offset at the TiN/ZrO_2 interface as well as on the trap depth was extracted. The model accurately describes the scaling of the leakage current with temperature and with thickness of the dielectric film, and it provides insight into the mutual interdependence of the competing transport mechanisms.**

***Index Terms*—DRAM, high-κ, leakage currents, Monte Carlo (MC) methods, thin-film capacitors, TiN, ZrO_2.**

I. Introduction

On downscaling of the storage capacitor of dynamic random access memory, tunneling currents through the insulating SiO_2 film increased and, finally, exceeded the leakage current criteria. Replacing SiO_2 with high-κ dielectrics has mitigated the problem by allowing for thicker insulating layers while maintaining the capacitance density. Many different materials have been investigated, e.g., Al_2O_3, HfO_2, ZrO_2, TiO_2, and $SrTiO_3$[1]–[3]. Among them, Zr-based dielectrics are currently favored [4]–[7], since ZrO_2 in its tetragonal phase has a very high permittivity of $\sim$40 and a sufficiently large bandgap of 5.4 eV, which suppresses quantum-mechanical tunneling currents. Since direct tunneling is not an issue, at least for the next chip generations, the focus is now on the reduction of the intrinsically high defect density in the aforementioned materials. The electronic states associated with these defects often lie within the bandgap and thus open up pathways for undesirable leakage currents. One strategy to reduce the defect density that has been pursued is defect passivation via doping with F or La [8]–[10].

Defect-assisted transport (DAT) has proven to be hard to model. Although the leakage current in the aforementioned materials has been studied extensively, the analysis has mostly remained on the level of simplified compact models [11]–[13]. These typically account only for certain aspects of the observed transport and neglect other essential parts. The widely used model for Poole–Frenkel (PF) conduction [14, eq. (3)], for example, describes the field-enhanced thermal emission of trapped electrons from defect states into the conduction band. However, electron injection into the defects is not considered, i.e., transport is implicitly assumed to be purely bulk limited. For HfO_2, a tunneling-assisted PF conduction mechanism has been proposed, which accounts for the injection step but does not include the position-dependent alignment of defect levels with respect to the electrode Fermi level upon an applied bias [15].

In summary, existing models usually fail to provide a complete picture of transport. Neither do they take into account that transport is mostly a multistep process nor do they include the competition between parallel conduction channels, e.g., different transport mechanisms, leading to their mutual interdependence.

A kinetic Monte Carlo (kMC) algorithm for the description of carrier transport through high-κ dielectrics was therefore developed [16]. It can handle tunneling transport within the bandgap (including DAT, which is often predominant in high-κ dielectrics). This versatile approach promises to remove the aforementioned restrictions. In the present work, our kMC algorithm is used to study leakage currents through TiN/high-κ-ZrO_2/TiN (TZT) metal–insulator–metal (MIM) structures. Identification of the most important transport channels is intended to support the undergoing experimental efforts toward system optimization and to outline potential for further scaling of the capacitor.

Section II introduces the basic ideas of kMC simulations, followed by a description of the simulation algorithm itself. Section III provides details on the fabrication of the investigated capacitors and the leakage data acquisition. Finally, in Section IV, the kMC simulation results are compared to experimental leakage current data from TZT capacitors. A transport model for this material system is established, and its implications are discussed.

II. kMC Simulations

Leakage currents in TZT capacitors were simulated using kMC. In these structures, conduction is dominated by DAT.

Manuscript received August 10, 2010; revised October 20, 2010; accepted October 22, 2010. Date of publication December 3, 2010; date of current version January 21, 2011. This work was supported by the German Excellence Initiative via the Nanosystems Initiative Munich. The review of this paper was arranged by Editor M. J. Kumar.

G. Jegert and P. Lugli are with the Institute for Nanoelectronics, Department of Electrical Engineering and Information Technology, Technical University of Munich, 80333 Munich, Germany (e-mail: guntherjegert@mytum.de; lugli@nano.ei.tum.de).

A. Kersch is with the Munich University of Applied Sciences, 80335 Munich, Germany (e-mail: alfred.kersch@hm.edu).

W. Weinreich is with the Fraunhofer Center Nanoelectronic Technology, 01099 Dresden, Germany (e-mail: wenke.weinreich@cnt.fraunhofer.de).

Color versions of one or more of the figures in this paper are available online at http://ieeexplore.ieee.org.

Digital Object Identifier 10.1109/TED.2010.2090158

Thus, a 3-D approach has been chosen, as it allows us the resolution of the pointlike nature of both the charge carriers and the defects, giving a more realistic picture of the transport (see Fig. 1). Additionally, a 3-D treatment enables studies of spatially localized phenomena such as formation of percolation paths under electrical stress [17] and of effects of electrode roughness, giving rise to local electric field enhancement near convex apertures [18]. A full 3-D analysis of tunneling in the presence of interface roughness is currently being performed and will be reported later.

A. Basics

Our kMC algorithm performs transport simulations on the level of single charge carriers, whose trajectory is computed in a stochastic framework, as they cross the dielectric. Take for instance a charge carrier trapped in a localized defect state within the dielectric: The charge carrier can undergo different processes, in the following called transitions: 1) tunneling to a neighboring defect; 2) escape to one of the electrodes; and 3) thermal excitation into the conduction band. All of these possibilities have to be taken into account concurrently. They are viewed in terms of transition probabilities per unit time, i.e., transition rates. As there are usually many charge carriers, for example, N, at the same time in the dielectric, the temporal behavior of the system, i.e., the flow of the individual charge carriers, takes the form of a Markovian random walk in the $3N$-dimensional space of charge carrier distributions. Monte Carlo (MC) techniques are employed to numerically simulate these Markov processes [19].

As different charge carriers couple to each other not only via screened Coulomb interaction but also via the occupation of the defect states—excluding multiple occupation, they are either available for transport when unoccupied or unavailable when occupied–single-particle MC simulations are not sufficient to describe the transport. A Poisson solver was coupled to the kMC simulator (see Section II-D). Although charge carrier concentrations up to $\sim 3 \times 10^{17}$ cm^{-3} were found, their influence on the simulation result is of minor importance due to the efficient screening in the high-κ dielectric.

B. Problem Definition

The MIM structure is described as a cuboid-shaped volume V of dielectric material with two metal electrodes attached to opposing faces. Defects are randomly allocated in V. Within the electrodes, a continuous Fermi–Dirac distribution of the charge carriers is assumed. Upon entering V, charge carriers are discretized and, thenceforth, treated as pointlike particles with defined energy until they leave the dielectric. Their individual trajectories are simulated. The leakage current then equals the net number of charge carriers that pass the dielectric in a given time interval.

Since our studies focus on the TiN/ZrO_2 system, where hole transport is negligible due to the large valence band offset, we will, in the following, limit our discussion to electrons. Nonetheless, the method is equally applicable to holes. We neglect the time that electrons in the conduction band need to reach the anode, as it is small compared to the time needed by the tunneling processes [16].

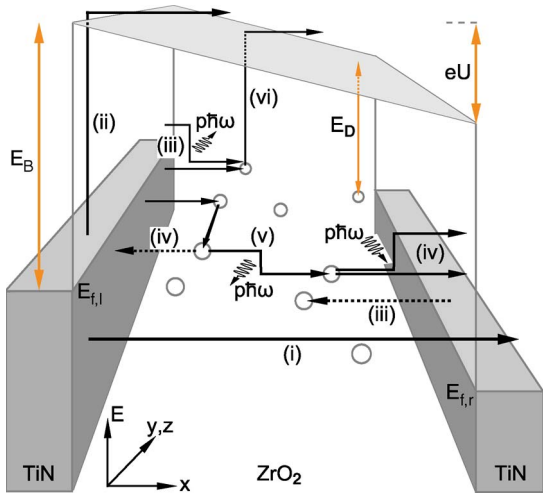

Fig. 1. Schematic band diagram of a MIM structure with applied voltage U. The most important charge transport mechanisms are (i) direct/Fowler–Nordheim tunneling, (ii) thermionic/Schottky emission, (iii) elastic or phonon-assisted tunneling into and (iv) out of defects, (v) defect-to-defect tunneling, and (vi) PF emission. p is the phonon number, and $\hbar\omega$ is the phonon energy.

Then, the problem we are dealing with may be outlined as follows: We are given a volume V of the dielectric material containing N_D defects, with $N_D = n_D \times V$, where n_D is the input defect density. Each defect site can accommodate, at most, one electron. The number of electrons N in V may change upon injection from or emission into the electrodes. These electrons can carry out M transitions T_μ $(1 \leq \mu \leq M)$. The set $\{T_\mu\}$ is made up of the following transitions, as shown in Fig. 1:

(i) direct/Fowler–Nordheim tunneling;
(ii) thermionic/Schottky emission;
(iii) elastic/phonon-assisted tunneling into a defect;
(iv) elastic or phonon-assisted tunneling out of a defect;
(v) elastic or phonon-assisted tunneling between defects;
(vi) PF emission out of a defect into the conduction band.

Details on the models for the transitions (i)–(vi) are provided in [16]. In Table I, typical transition rates are given for transitions involving a defect in a distance of 2 nm from the cathode. As can be seen, the transition rates vary over many orders of magnitude. This means that the fast events will occur very often and thus are simulated with high statistics. Rare events, however, i.e., those transitions which have lower rates, are not captured by the simulation. This is known as the time-scaling problem in kMC simulations [20]. The speed with which the kMC simulation advances in time, i.e., the time step width, is determined by the fast processes. Thus, if one is interested in studying the rare events, strategies to connect the different time scales have to be implemented in the simulation algorithm. We will deal with this issue in Section II-F.

C. MC Techniques

The MC procedure allows us to perform the single steps in the Markovian random walk, thus mimicking the electron

TABLE I
SELECTED TRANSITION RATES (IN PER SECOND) AT 25 °C FOR A DEFECT AT A DISTANCE OF 2 nm FROM THE CATHODE

type of transition	U=1V	U=3V
1) tunneling from cathode to empty defect	5.4×10^{-1}	3.0×10^{5}
2) tunneling from occupied defect to cathode	1.3×10^{6}	4.3×10^{4}
3) tunneling from occupied defect to anode	3.6×10^{-14}	4.6×10^{3}
4) PF emission into conduction band	1.0×10^{-2}	7.6×10^{1}

dynamics. Given an electron distribution at time t, we have to determine by which transition μ and after which time τ the system will pass into another state. In the following, we will closely follow the ideas of Gillespie [19] and adapt them to our system. We start by defining $R_\mu dt$ as the probability, to first order in dt, that a particular electron transition T_μ will take place in the next time interval dt. Here, R_μ is the transition rate associated with transition T_μ. The time step dt is required to be infinitesimal to ensure that the probability of another transition T_ν, $\nu \neq \mu$, occurring in the time interval dt is negligible. In order to derive a rigorous algorithm for simulating the time evolution of the system, we define the probability density function (pdf) $P(\tau, \mu)$ as

$P(\tau, \mu)d\tau =$ probability for an electron at time t to undergo a transition T_μ within the differential time interval $(t+\tau, t+\tau+d\tau)$.

$P(\tau, \mu)$ is a joint pdf on the space of the continuous variable τ $(0 \leq \tau < \infty)$ and the discrete variable μ (μ is a positive integer; $1 \leq \mu \leq M$). To correctly compute the stochastic dynamics of the electron distribution, we have to randomly choose a pair (τ, μ) according to $P(\tau, \mu)d\tau$, thus specifying the next step in the random walk. To derive an exact analytical expression for $P(\tau, \mu)$, we calculate $P(\tau, \mu)d\tau$ as the product of $P_0(\tau)$, the probability at time t that no transition will occur in the time interval $(t, t+\tau)$, and $R_\mu d\tau$

$$P(\tau, \mu)d\tau = P_0(\tau)R_\mu d\tau \tag{1}$$

where $P_0(\tau)$ can be calculated as

$$P_0(\tau) = e^{-R\tau}. \tag{2}$$

Here, $R \equiv \sum_{\mu=1}^{M} R_\mu$ is the cumulative transition rate. Equation (2) simply describes the exponential decay of the existing state through all available transition channels [19]. Inserting (2) into (1) delivers

$$P(\tau, \mu) = \begin{cases} R_\mu e^{-R\tau}, & \text{if } \tau \in [0, \infty),\ 1 \leq \mu \leq M \\ 0, & \text{otherwise.} \end{cases} \tag{3}$$

We continue by writing the two-variable pdf as a product of two one-variable pdfs

$$P(\tau, \mu) = P_1(\tau) \times P_2(\mu|\tau) \tag{4}$$

where $P_1(\tau)d\tau$ is the probability that the next transition will occur between $t+\tau$ and $t+\tau+d\tau$, irrespective of which transition it might be. $P_2(\mu|\tau)$ is the probability that it will be a T_μ transition, given that the transition occurs between $t+\tau$ and $t+\tau+d\tau$. Using (3) and (4) and the addition theorem for probabilities [19], we obtain

$$P_1(\tau) = \sum_{\mu=1}^{M} P(\tau, \mu) = R \cdot e^{-R\tau} \tag{5}$$

$$P_2(\mu|\tau) = \frac{P(\tau, \mu)}{P_1(\tau)} = \frac{R_\mu \cdot e^{-R\tau}}{R \cdot e^{-R\tau}} = \frac{R_\mu}{R}. \tag{6}$$

The idea for the MC step is to first generate a random number value τ according to $P_1(\tau)$, which determines the time at which the next transition will occur, and then to generate a random integer μ according to $P_2(\mu|\tau)$, to select the actual process responsible for the transition. The resulting pair (τ, μ) will be distributed according to $P(\tau, \mu)$. Gillespie presented a straightforward procedure on how to construct random numbers distributed according to any prescribed pdf from random numbers uniformly distributed in the unit interval (see [19, Appendix]). Thus, the MC step reduces to the generation of two random numbers r_1 and r_2 from the uniform distribution in the unit interval. The lifetime τ of the system state is then calculated by

$$\tau = -\ln(r_1)/R \tag{7}$$

and the transition μ is chosen so that

$$\sum_{\mu'=1}^{\mu-1} R_{\mu'} < r_2 \sum_{\mu'=1}^{M} R_{\mu'} = r_2 R \leq \sum_{\mu'=1}^{\mu} R_{\mu'}. \tag{8}$$

D. Poisson's Equation

In general, the transition probabilities can be a function of the electron density (e.g., in the defect states) and of the electrostatic potential. Thus, to self-consistently simulate the system dynamics with kMC, Poisson's equation has to be solved at each MC step. The solution is carried out in a finite-element scheme [21], which allows adaptive grid refinement in regions of large electric field gradients, as they are found around charges stored in the dielectric. This will, in the future, also allow us to study the effects of interface roughness.

E. Algorithm

Using these MC techniques, implementation of the kMC algorithm is straightforward. It may be outlined as follows.

1) Set time variable $t = 0$, and specify the initial electron distribution by assigning N electrons to the N_D defect states. Solve Poisson's equation on volume V, and calculate rates R_μ for all possible transitions. They collectively determine the pdf. Specify sampling times at which the current flow is evaluated and a stopping time t_{stop} at which the simulation ends. Independence of the initial conditions has to be assured.
2) Generate a pair of random numbers (r_1, r_2), and using (7) and (8), calculate the corresponding pair (τ, μ).

3) Advance t by τ, and carry out electron transition T_μ, i.e., change electron distribution accordingly.
4) Solve Poisson's equation, and recalculate transition rates.
5) If t has been advanced through a sampling point, read out current. Check if the current has reached a constant level. If $t \geq t_{\mathrm{stop}}$, terminate calculation; otherwise, return to step 2).

F. Time-Scaling Problem

While the algorithm sketched in Section II-E is fairly straightforward, in practice, problems arise due to the fact that the transition rates range over many orders of magnitude (see Table I). It may happen that the major part of the computing time is used for the simulation of the fast events, while the rare events, associated with slow rates, are not captured by the simulation. Often, these rare events are of particularly high interest [20]. Thus, the algorithm should include a strategy to bridge the time scales, allowing one to access all of them.

A simulation run starts with all possible transitions being allowed. After having executed a sufficient number of kMC iterations, the algorithm identifies the most frequent events, i.e., transitions T_ξ with R_ξ larger than a specified cutoff rate R_{cutoff}, and removes them from the simulation. Their effect on both current flow and electron distribution in the dielectric is, in the following, taken into account in the form of averaged values, extracted from the previous kMC iterations. Take for instance a defect state close to an electrode: As can be concluded from Table I, it will be frequently populated by electrons being injected from the electrode, and it will be depopulated by the same electrons being reemitted to the electrode (transitions 1) and 2) in Table I). To save computation time, these individual transitions are removed. Instead of resolving the fast fluctuations of the defect occupation between zero and one, we calculate the occupation probability f of the defect as ratio of time for which the defect has been occupied to the time for which it has been unoccupied. Before each kMC iteration, either the defect will be occupied by an electron with a probability f or it will be unoccupied with a probability $(1-f)$. f is subsequently used as a weighting factor for other transitions involving this defect. Following this scheme, the time steps of the kMC simulation can be increased stepwise by decreasing R_{cutoff}. The resulting inaccuracies due to this procedure were found to be negligible, as the Coulomb interaction between the charge carriers is screened very efficiently in the high-κ material.

III. Sample Growth

For the fabrication of the capacitors, (001)-silicon wafers were coated with a bottom electrode consisting of 10 nm of chemical-vapor-deposited TiN ($TiCl_4, NH_3$), grown at 550 °C [22]. Subsequently, the ZrO_2 film was grown by atomic layer deposition (TEMAZ, O_3) at 275 °C. The top TiN electrode was deposited at 450 °C by chemical vapor deposition. Temperature-dependent current measurements were carried out on a heatable wafer holder with a Keithley 4200 parameter analyzer and delay times of 2 s. We believe that, below ~1.3 V, transient currents, which arise due to the applied voltage ramp (0.05 V/s), dominate over the steady-state leakage. These were not considered in the analysis of the measured leakage currents in [16]. In agreement with [23], we assume that the transient currents consist of dielectric relaxation currents and charging/discharging phenomena like charge trapping/detrapping involving defect states in the ZrO_2 bandgap. These currents typically only weakly depend on the temperature [23], as it is observed here [see Fig. 2(a)].

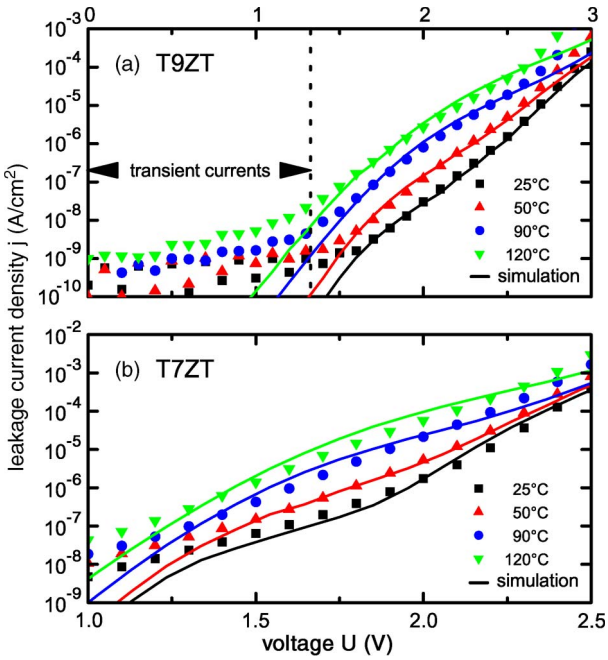

Fig. 2. (Symbols) Leakage current data of (a) TZ9T and (b) TZ7T capacitors compared to (lines) kMC simulation results. In the low-voltage region [exemplarily shown in (a)], no comparison between experiment and simulation is possible, as here, the measured current seems to be dominated by transient currents, while the kMC results describe the steady state. Dielectric breakdown was observed for $U \geq 3.2$ V and $U \geq 2.6$ V (not shown).

IV. Results and Discussion

TZT capacitors with 9- (TZ9T) and 7-nm-thick (TZ7T) ZrO_2 layers were investigated. Measured κ values of 38 for both capacitors evidence that the ZrO_2 is fully crystallized in the tetragonal phase. Current–voltage characteristics of both capacitors for temperatures between 25 °C and 120 °C are shown in Fig. 2. Dielectric breakdown of the samples occurred at voltages of 3.2 and 2.6 V (not shown). While a strong temperature dependence of the current was observed for voltages below 2.5 and 2 V, above these values, the leakage current scales weaker with temperature. Particularly for lower temperatures, the slope of the curves increases.

A leakage current model for the TZT capacitors, as it followed from kMC simulations, was briefly sketched in [16]. In the present work, we present a more elaborate evaluation and discussion of the model and its implications. Thickness scaling of the leakage current is discussed, as well as contributions from different defect positions x (see Fig. 3) to the leakage current. We analyze the mutual interdependence of the competing conduction mechanisms and test our model with respect to its sensitivity toward changes of the crucial model parameters.

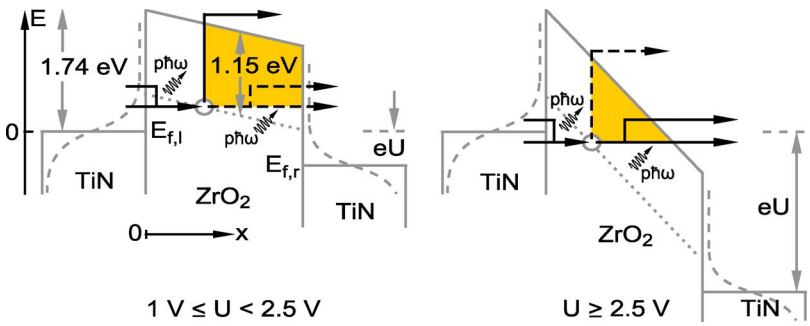

Fig. 3. Schematic band structure of a TZT capacitor for (left side) low and (right side) high voltages. Arrows illustrate electron flow, whereas a dashed arrow indicates that this electron emission path is slower than the other one. Barriers for tunnel emission are highlighted with color.

A. Leakage Current Model

The kMC simulations for the aforementioned MIM structures, whose leakage current curves are shown in Fig. 2, were carried out using best estimate physical parameters from experiment and theory. The full set of employed model parameters was given in [16]. To avoid ambiguities in the interpretation of the experimental data, we have chosen the simplest model which describes the essential features of the measured currents. A single defect level and a uniform defect distribution in the dielectric were assumed. The model was calibrated on the TZ9T capacitor.

Very good agreement between simulation (lines) and experiment (symbols) was achieved, particularly in terms of the temperature dependence of the leakage current [Fig. 2(a)]. The same parameter set was used to simulate the TZ7T capacitor. As shown in Fig. 2(b), thickness scaling of the leakage current is modeled very accurately. The experimental data are closely fitted, and in particular, the more pronounced increase of the slope of the current curves (here at ∼2 V), compared to the TZ9T capacitor, is reproduced.

The transport model is shown in Fig. 3. We assumed a defect density of $n_D = 3 \cdot 10^{18}$ cm^{-3}. For the TZ9T capacitor, for voltages below 2.5 V, the leakage current was found to be dominated by PF emission of electrons from positively charged defects with a depth $E_D = 1.15$ eV with respect to the ZrO_2 conduction band. Electrons are injected from the TiN cathode into the defects via elastic and multiphonon-assisted tunneling. Detrapping occurs in a next step via PF emission into the ZrO_2 conduction band, where the electrons quickly flow to the anode. Thermally activated detrapping of electrons is the transport limiting step in this multistep process. Thus, it governs the temperature scaling of the current, which is found to be strong in this voltage range. As the kMC simulations, in contrast to standard treatments, account for the injection step, it is possible to extract information on the conduction band offset E_B between TiN and ZrO_2, which was found to be 1.74 eV. Thus, the defect level lies well above the electrode Fermi level, suggesting a limitation of the current flow due to the low occupation probability of the defect states. In this sense, the current is electrode limited, explaining the failure of the standard PF formula in describing the leakage current [16], since the latter implies a bulk limitation of transport. This point will be further discussed hereinafter. For $U > 2.5$ V, at lower temperatures ($T \leq 50$ °C), an increase of the slope of the current–voltage curves was observed together with a reduced temperature scaling. Here, the dominant conduction mechanism changes from PF emission to tunnel emission, also called trap-assisted tunneling (TAT), i.e., electrons predominantly escape from the defect states via tunneling through the potential barrier. At high voltages when the shape of this barrier changes from trapezoidal to triangular (see Fig. 3), the rate for this mechanism strongly increases with the applied voltage so that it finally surpasses the rate for PF emission. The stronger voltage dependence of the only weakly temperature-dependent TAT explains the increased slope. For $T \geq 90$ °C, the rate for PF emission is higher than the one for TAT over the whole voltage range so that PF emission dominates the leakage current. We note again that, below ∼1.3 V, transient currents dominate, most probably dielectric relaxation currents and charge trapping/detrapping. However, it is possible that a transport channel not captured by our model is present, e.g., one involving a second defect type. A fit of this voltage region with the implemented transport mechanisms, listed in Section II-B, was not possible. The analysis of transient leakage data, as suggested in [24], in the future should shed light on this. In general, the modeling of leakage current is a complex problem with many unknowns, particularly in case of DAT. Thus, further thorough experimental investigation is needed in order to complement the present investigation and test the transport model, e.g., deep-level transient spectroscopy [25] to study the spatial and energetic defect distribution.

B. Contributions From Different Defect Positions

In the presence of an electric field, the energetic alignment of the defect states with respect to the cathode Fermi level $E_{f,l}$ depends on their distance from the electrode. Simulations show that, varying U, different defect positions deliver the largest current contribution (see Figs. 4 and 5).

In Fig. 4, the simulated leakage current for the TZ9T capacitor at 25 °C is shown (continuous line). Contributions of defects to the leakage current have been resolved with respect to their position x. Additionally, Fig. 5 exemplarily shows the occupation probability f of defects at $x = 2$ nm and $x = 4$ nm as a function of U. For $U \sim 1$ V, defects deeper in the dielectric, with $x = 3.5{-}4.0$ nm, give the highest current contribution, as they are nearly on a level with $E_{f,l}$. Nonetheless, f stays below 10^{-3}, since electron injection is quite slow, particularly slower than electron extraction via PF emission, which depopulates the

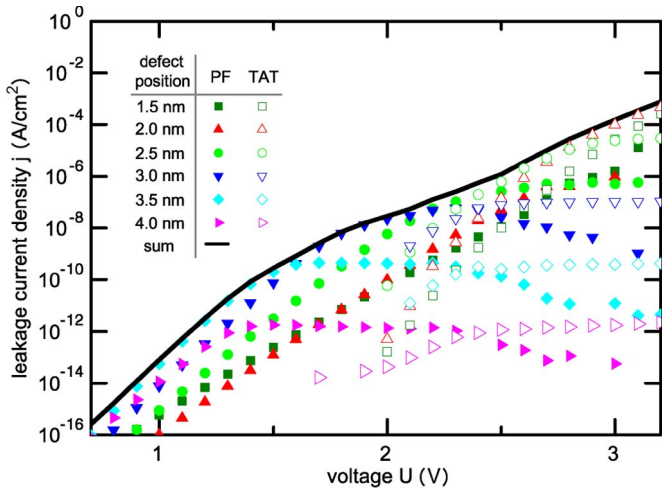

Fig. 4. Leakage current of the TZ9T capacitor at 25 °C. Current contributions of traps, lying at distances $x = 1.5{-}4$ nm of the cathode, are shown. Filled symbols indicate transport via PF emission, and empty symbols indicate transport via TAT.

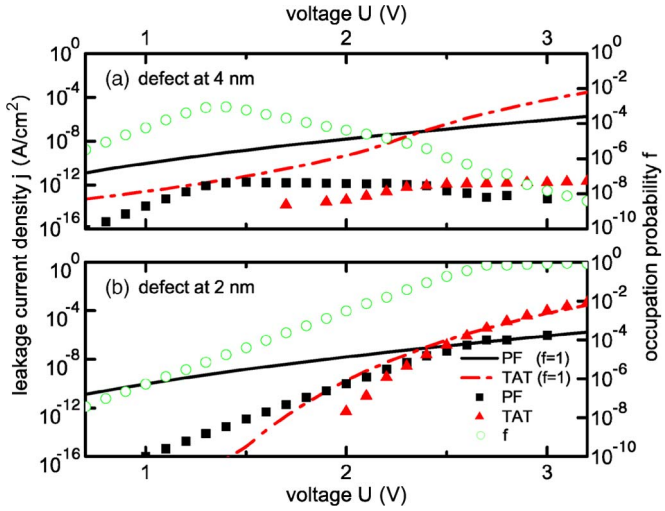

Fig. 5. Occupation probability versus voltage of defects at (a) $x = 2$ nm and (b) $x = 4$ nm is shown. Lines show upper limits for their current contributions, assuming $f = 1$ for all voltages. Symbols indicate simulated currents.

defects. Contributions from defects lying even deeper in the dielectric are suppressed due to the very slow electron injection, while contributions from interface-near defects are low, since these lie well above $E_{f,l}$. Tunneling into these defects is very fast; however, reemission into the cathode is even faster, as Table I shows, leading for defects at $x = 2$ nm to a low occupation $f \sim 10^{-6}$. For $U \sim 2$ V, defects closer to the cathode are gradually aligned with $E_{f,l}$; thus, their occupation rises, as can be seen in Fig. 5(b). Here, defects at 2.5–3.0 nm give the highest contribution to the current. At 2.5 V, the dominant transport mechanism changes from PF emission to TAT, i.e., tunnel emission. In this case, defects between 2.0 and 2.5 nm, being nearly fully occupied, deliver the highest current contribution. Fig. 5 also shows the theoretical maxima for the current contributions (lines) of the defects. Full occupation is assumed, i.e., $f = 1$, independent of U. The real contributions (symbols), as discussed, are roughly obtained by multiplying the theoretical maxima with f. Particularly for low voltages, the current, in this sense, is injection limited.

Furthermore, Fig. 4 shows the mutual interdependence of the parallel transport channels. At voltages where TAT dominates the leakage current, a drop of the PF current can be observed, although the PF emission rate still increases. In this voltage region, electrons are very efficiently extracted from the defects via tunneling and, thus, are no longer available for PF emission. The defect occupation decreases [see Fig. 5(a)]. Clearly, the competition between the two transport channels alters their individual characteristics.

As transport across interface-near defects is suppressed, for further scaling of these ZrO_2 films, defects in the bulk have to be minimized. Concerning electrode roughness, the leakage current is expected to be rather insensitive to the local electric field enhancement near convex apertures. For extremely thin films, however, the more important consequence of electrode roughness is the local thinning of the dielectric film. Then, TAT, depending exponentially on the tunneling barrier thickness, is expected to strongly increase, as well as the sensitivity of the leakage current toward electrode roughness. This will be discussed in detail in a future publication.

C. Sensitivity Analysis

The most crucial simulation parameters, which were attuned in order to reproduce the leakage current data of the TZT capacitors, are the conduction band offset E_B between TiN and ZrO_2 and the defect depth E_D. We varied them systematically to investigate the sensitivity of our model.

In Fig. 6(a), simulation results for a fixed $E_B = 1.74$ eV and varying $E_D = 0.95{-}1.25$ eV are shown. For 25 °C, the leakage current is maximum for $E_D = 1.05$ eV, while it is lower going to shallower or deeper defects. The shallower a defect is, the higher the rate for PF emission of trapped electrons. The occupation probability, however, is lower due to the higher energy difference to $E_{f,l}$. For deeper defects, the occupation probability is high, while the PF emission rate is low. Thus, the existence of a maximum is expected. Temperature scaling of the leakage current is found to be stronger for deeper defects, as expected for the thermally activated PF emission. Increasing E_D, the transition from PF conduction to TAT, visible as change in the slope, occurs at lower voltages, for the depicted set of defect depths best seen comparing $E_D = 1.25$ eV and $E_D = 1.15$ eV. Thus, the temperature scaling of the leakage current and the change of the dominant conduction mechanism can be used to determine E_D, given E_B. In Fig. 6(b), the simulation results for a fixed $E_D = 1.15$ eV and varying $E_B = 1.54{-}1.84$ eV are shown. For lower E_B, particularly at lower voltages, where none of the defects are aligned with $E_{f,l}$, the current rises, since the defects are pushed closer to $E_{f,l}$ and their occupation probability thus rises. The effect is more pronounced at 120 °C, as the leakage current here is mainly limited by the low occupation of the defects, while at 25 °C, it is limited by the slow PF emission. Thus, changing the band offset also changes the temperature scaling of the leakage current.

Consequently, without further information on E_B, E_D, or the defect density n_D, the triplet (n_D, E_B, E_D), extracted from the kMC simulations, is not completely unambiguous. However, as soon as one of these values is fixed, the others can be determined with high accuracy. We have chosen to fix n_D to

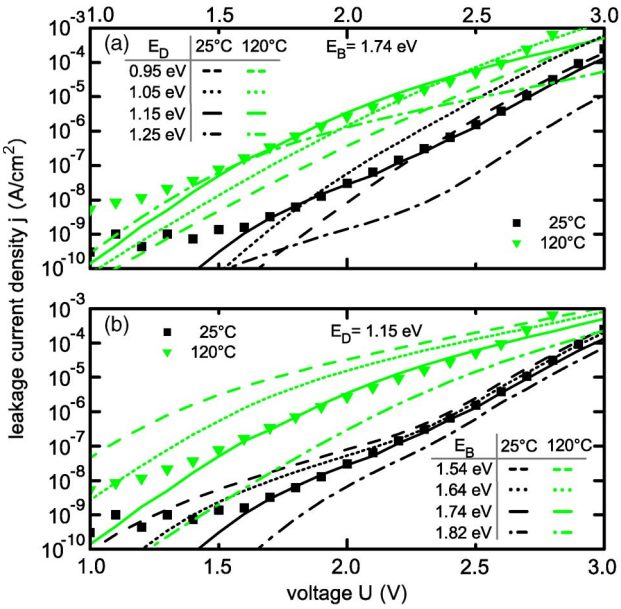

Fig. 6. Leakage current data of the TZ9T capacitor for 25 °C and 120 °C (symbols). Simulated currents for (a) fixed $E_B = 1.74$ eV and varying E_D and (b) fixed $E_D = 1.15$ eV and varying E_B are shown. As in Fig. 2, the low-voltage region, dominated by transient currents, is not shown.

$3 \cdot 10^{18}$ cm^{-3}, resulting in $E_B = 1.74$ eV, a reasonable value for the band offset [16], and $E_D = 1.15$ eV, a defect level that might be ascribed to oxygen vacancies [26].

V. Conclusion

Based on kMC simulations, a self-consistent leakage current model for TiN/ZrO_2/TiN capacitors was developed. kMC proved to be a useful technique for studying the mutual interdependence of parallel transport channels. Most importantly, electron injection into defect states is accounted for. In contrast to the pure bulk limitation of the transport suggested by the standard PF model, the conduction band offset between TiN and ZrO_2 turns out to strongly limit the conduction. Bulk defects at a distance of 2–4 nm from the injecting electrode are found to deliver the main current contribution. These results strongly suggest an optimization of the electrode work function and a reduction of the bulk defect density as a viable strategy for decreasing the leakage currents. More experimental data (for instance on the nature of the traps) would be needed for a full validation of the theoretical transport model adopted here.

Acknowledgment

Financial support of the German Excellence Initiative via the Nanosystems Initiative Munich (NIM) is gratefully acknowledged.

References

[1] T.-M. Pan, C.-I. Hsieh, T.-Y. Huang, J.-R. Yang, and P.-S. Kuo, "Good high-temperature stability of TiN/Al_2O_3/WN/TiN capacitors," *IEEE Electron Device Lett.*, vol. 28, no. 11, pp. 954–956, Nov. 2007.

[2] N.-J. Son, Y. Oh, W. Kim, S.-M. Jang, W. Yang, G. Jin, D. Park, and K. Kim, "A unique dual-poly gate technology for 1.2-V mobile DRAM with simple in situ n^+-doped polysilicon," *IEEE Trans. Electron Devices*, vol. 51, no. 10, pp. 1644–1652, Oct. 2004.

[3] S. K. Kim, G.-J. Choi, S. Y. Lee, M. Seo, S. W. Lee, J. H. Han, H.-S. Ahn, S. Han, and C. S. Hwang, "Al-doped TiO_2 films with ultralow leakage currents for next generation DRAM capacitors," *Adv. Mater.*, vol. 20, no. 8, pp. 1429–1435, Apr. 2008.

[4] A. Berthelot, C. Caillat, V. Huard, S. Barnola, B. Boeck, H. Del-Puppo, N. Emonet, and F. Lalanne, "Highly reliable TiN/ZrO_2/TiN 3D stacked capacitors for 45 nm embedded DRAM technologies," in *Proc. Solid-State Device Res. Conf.*, Sep. 2006, pp. 343–346.

[5] H. J. Cho, Y. D. Kim, D. S. Park, E. Lee, C. H. Park, J. S. Jang, K. B. Lee, H. W. Kim, Y. J. Ki, I. K. Han, and Y. W. Song, "New TIT capacitor with $ZrO_2/Al_2O_3/ZrO_2$ dielectrics for 60 nm and below DRAMs," *Solid State Electron.*, vol. 51, no. 11/12, pp. 1529–1533, Nov./Dec. 2007.

[6] Y.-H. Wu, C.-K. Kao, B.-Y. Chen, Y.-S. Lin, M.-Y. Li, and H.-C. Wu, "High density metal-insulator-metal capacitor based on $ZrO_2/Al_2O_3/ZrO_2$ laminate dielectric," *Appl. Phys. Lett.*, vol. 93, no. 3, p. 033 511, Jul. 2008.

[7] S. Monaghan, K. Cherkaoui, E. O'Connor, V. Djara, P. K. Hurley, L. Oberbeck, E. Tois, L. Wilde, and S. Teichert, " TiN/ZrO_2/Ti/Al metal-insulator-metal capacitors with subnanometer CET using ALD-deposited ZrO_2 for DRAM applications," *IEEE Electron Device Lett.*, vol. 30, no. 3, pp. 219–221, Mar. 2009.

[8] K. Tse and J. Robertson, "Defect passivation in HfO_2 gate oxide by fluorine," *Appl. Phys. Lett.*, vol. 89, no. 14, p. 142 914, Oct. 2006.

[9] T. Schimizu and M. Koyama, "Control of electronic properties of HfO_2 with fluorine doping from first-principles," *Appl. Surf. Sci.*, vol. 254, no. 19, pp. 6109–6111, Jul. 2008.

[10] D. Liu and J. Robertson, "Passivation of oxygen vacancy states and suppression of Fermi pinning in HfO_2 by La addition," *Appl. Phys. Lett.*, vol. 94, no. 4, p. 042 904, Jan. 2009.

[11] S. H. Lin, K. C. Chiang, A. Chin, and F. S. Yeh, "High-density and low-leakage-current MIM capacitor using stacked TiO_2/ZrO_2 insulators," *IEEE Electron Device Lett.*, vol. 30, no. 7, pp. 715–717, Jul. 2009.

[12] Y. Seo, S. Lee, I. An, C. Song, and H. Jeong, "Conduction mechanism of leakage current due to the traps in ZrO_2 thin film," *Semicond. Sci. Technol.*, vol. 24, no. 11, p. 115 016, Oct. 2009.

[13] S. Chakraborty, M. K. Bera, G. K. Dalapati, D. Paramanik, S. Varma, P. K. Bose, S. Bhattacharya, and C. K. Maiti, "Leakage current characteristics and the energy band diagram of Al/$ZrO_2/Si_{0.3}Ge_{0.7}$ hetero-MIS structures," *Semicond. Sci. Technol.*, vol. 21, no. 4, pp. 467–472, Feb. 2006.

[14] J. R. Yeargan and H. L. Taylor, "The Poole-Frenkel effect with compensation present," *J. Appl. Phys.*, vol. 39, no. 12, pp. 5600–5604, Nov. 1968.

[15] D. S. Jeong and C. S. Hwang, "Tunneling-assisted Poole-Frenkel conduction mechanism in HfO_2 thin films," *J. Appl. Phys.*, vol. 98, no. 11, p. 113 701, Dec. 2005.

[16] G. Jegert, A. Kersch, W. Weinreich, U. Schröder, and P. Lugli, "Modeling of leakage currents in high-κ dielectrics: Three-dimensional approach via kinetic Monte Carlo," *Appl. Phys. Lett.*, vol. 96, no. 6, p. 062 113, Feb. 2010.

[17] D. Zhou, U. Schröder, G. Jegert, M. Kerber, S. Uppal, R. Agaiby, M. Reinicke, J. Heitmann, and L. Oberbeck, "Time dependent dielectric breakdown of amorphous $ZrAl_xO_y$ high-k dielectric used in dynamic random access memory metal-insulator-metal capacitor," *J. Appl. Phys.*, vol. 106, no. 4, p. 044 104, Aug. 2009.

[18] Y.-P. Zhao, G.-C. Wang, T.-M. Lu, G. Palasantzas, and J. T. M. De Hosson, "Surface-roughness effect on capacitance and leakage current of an insulating film," *Phys. Rev. B, Condens. Matter*, vol. 60, no. 12, pp. 9157–9164, Sep. 1999.

[19] D. T. Gillespie, "A general method for numerically simulating the stochastic time evolution of coupled chemical reactions," *J. Comput. Phys.*, vol. 22, no. 4, pp. 403–434, Dec. 1976.

[20] F. Rossi, P. Poli, and C. Jacoboni, "Weighted Monte Carlo approach to electron transport in semiconductors," *Semicond. Sci. Technol.*, vol. 7, no. 8, pp. 1017–1035, May 1992.

[21] W. Bangerth, R. Hartmann, and G. Kanschat, "deal.II—A general purpose object oriented finite element library," *ACM Trans. Math. Softw.*, vol. 33, no. 4, p. 27, Aug. 2007.

[22] W. Weinreich, R. Reiche, M. Lemberger, G. Jegert, J. Müller, L. Wilde, S. Teichert, J. Heitmann, E. Erben, L. Oberbeck, U. Schröder, A. J. Bauer, and H. Ryssel, "Impact of interface variations on J–V and C–V polarity asymmetry of MIM capacitors with amorphous and crystalline $Zr_{(1-x)}Al_xO_2$ films," *Microelectron. Eng.*, vol. 86, no. 7–9, pp. 1826–1829, Mar. 2009.

[23] V. K. Gueorguiev, P. V. Aleksandrova, T. E. Ivanov, and J. B. Koprinarova, "Hysteresis in metal insulator semiconductor

structures with high temperature annealed ZrO_2/SiO_x layers," *Thin Solid Films*, vol. 517, no. 5, pp. 1815–1820, Jan. 2009.
[24] G. W. Dietz and R. Waser, "How to analyse relaxation and leakage currents of dielectric thin films: Simulation of voltage-step and voltage-ramp techniques," *Integr. Ferroelectr.*, vol. 9, pp. 317–332, Aug. 1995.
[25] D. V. Lang, "Deep-level transient spectroscopy: A new method to characterize traps in semiconductors," *J. Appl. Phys.*, vol. 45, no. 7, pp. 3023–3032, Jul. 1974.
[26] J. Robertson, K. Xiong, and B. Falabretti, "Point defects in ZrO_2 high-κ gate oxide," *IEEE Trans. Device Mater. Rel.*, vol. 5, no. 1, pp. 84–89, Mar. 2005.

Gunther Jegert was born in Usingen, Germany, in 1981. He received the Dipl.-Phys. degree in physics from the Technische Universität München (TUM), Munich, Germany, in 2007, for his work on GaN quantum dots as optical transducers for chemical sensors. He is currently working toward the Ph.D. degree in physics in the Institute for Nanoelectronics, Department of Electrical Engineering and Information Technology, TUM.

Since 2008, he has been with the Institute for Nanoelectronics. His research focuses on the modeling and simulation of transport in nanostructures and reliability analysis in high-κ dielectrics. His current research interests also involve the simulation of photocurrent generation in organic solar cells.

Alfred Kersch received the Ph.D. degree in theoretical physics from the University of Mainz, Mainz, Germany, in 1990.

He then joined the Corporate Research of Siemens AG, the Memory Product Division of Infineon AG in 1999, and the Product Division of Qimonda AG in 2006. Since 2009, he has been with the Munich University of Applied Sciences, Munich, Germany. His research interests involve modeling and simulation of microstructures and nanostructures, the methods of fabrication, and the *ab initio* calculation of high-κ dielectric properties.

Wenke Weinreich was born in Burgstädt, Germany, in 1981. She received the Dipl.-Nat. degree in applied natural sciences from the Technische Universität Bergakademie Freiberg, Freiberg, Germany, in 2005, for her work on the wet chemical etching behavior and mechanism studies of multicrystalline silicon in HF/HNO_3 used in solar industry. She is currently working toward the Ph.D. degree in electrical engineering at the Fraunhofer Center Nanoelectronic Technology, Dresden, Germany.

Since 2006, she has been with the Fraunhofer Center Nanoelectronic Technology. Her research focuses on the atomic layer deposition of high-κ dielectrics and the physical and electrical characterization with regard to the application in MIM capacitors for DRAMs.

Paolo Lugli (SM'07) received the Laurea degree in physics from the University of Modena, Modena, Italy, in 1979 and the M.Sc. and Ph.D. degrees in electrical engineering from Colorado State University, Fort Collins, in 1982 and 1985, respectively.

In 1993, he was appointed as a full Professor of optoelectronics with the Universita di Roma "Tor Vergata," Rome, Italy. Since 2002, he has been with the Technische Universität München, Munich, Germany, as the Head of the newly created Institute for Nanoelectronics. His current research interests involve modeling and simulation of nanostructures, as well as the realization and characterization of organic devices.